ORIGINAL PAPER

Energy Utilization and Kinetic Characteristics Due to Plasma-Catalytic Synergy Effect with Reactant Structurally Bond Strength and Inductive Effect

Chen-Jui Liang[1] · Kuan-Yu Huang[2]

Abstract

The energy utilization and kinetic characteristics in pulsed bipolar plasma catalysis of organic reactants were investigated. A kinetic theoretical formula was established for depicting the plasma dissociation and synergistic catalysis. The synergy factors of $C_5 - C_{10}$ n-alkanes were independent of the number of secondary hydrogens, but for $(CH_3)_m$-benzenes ($m = 0 - 3$), as the number of methyl groups increased, the synergy factors slightly increased. The rate of increase in energy utilization due to the synergy effect was inversely proportional to the reactivity of reactants. Some energy from plasma discharge was wasted at low conversion until the catalytic activity began to play a role. The energy utilization increased considerably once the catalytic effect was activated. However, when the reactant was close to its complete oxidation, the plasma dissociation and catalysis reactions competed with each other, leading to wastage of some of the energy. These phenomena were more remarkable for the alkanes than for the aromatics.

Graphic Abstract
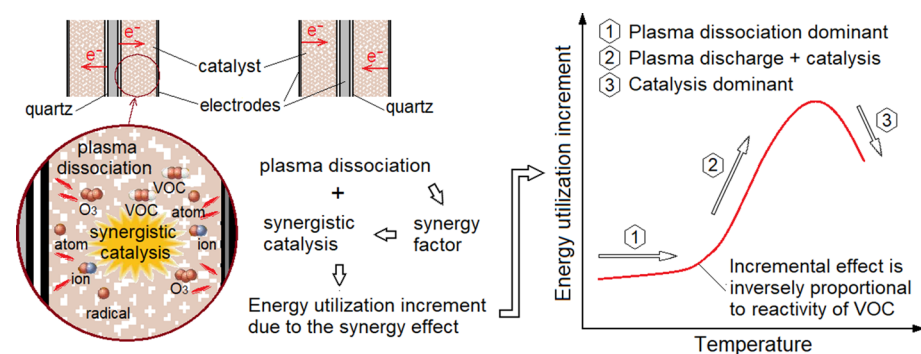
Pulsed bipolar plasma catalysis and energy use mechanism

Keywords Plasma-driven catalysis · Multi-metallic oxides · Reaction mechanisms · Air pollution control

---

Extended author information available on the last page of the article

Introduction

High-concentration alkanes and aromatics are widely present in vehicular and industrial exhaust gases. [1–4] The carbon numbers of these compounds are usually between 5 and 10, which implies that they represent the dominant components of ambient volatile organic compounds (VOCs). [5, 6] Ambient VOCs severely affect human health, [7, 8] especially owing to their poisoning effect. [9] Existing organic waste gas removal technologies are mainly based on activated carbon adsorption, [10] catalyst incineration, [11] and thermal incineration. [12] Atmospheric-pressure nonthermal plasma-catalytic processing is one of the most promising technologies for removing VOCs from exhaust gases. [13]

Plasma-enhanced catalysis (PEC) and plasma-driven catalysis (PDC) are two common plasma catalysis systems. [14] The PEC system uses a nonthermal plasma (NTP) reactor and a catalytic reactor in series to achieve complementary effects. [15] Ozone is generated by the NTP reactor, and this ozone accelerates VOC decomposition in the downstream catalyst bed. [16, 17] Jarrige and Vervisch [18] investigated the PEC of propane and isopropyl alcohol at ambient temperature over Al_2O_3–MnO_2 catalyst. Lin et al. [19] combined NTP, adsorption, and catalysis to remove C_3F_8. In a previous study, we investigated the kinetic characterization of high-concentration VOCs in the PEC system. [20] In the PDC system, the catalyst is placed in the NTP reactor and directly activated through NTP. [21] Kim et al. [22] investigated VOC decomposition by using flow-type PDC over different metallic catalysts (Ag, Ni, Pt, Pd) in conjunction with TiO_2, $α$-Al_2O_3, or zeolite as the catalyst supporter. Kim and Ogata [23] used an intensified charged coupled device camera to visualize the interaction of discharge plasma with catalyst at atmospheric pressure and ambient temperature. In a previous study, we determined the kinetics of energy synergy in the pulsed bipolar plasma-catalytic reaction of VOCs. [24] Li et al. [25] reviewed recent advances related to the use of dielectric barrier discharge plasma in catalysis.

The chemical and physical interactions between plasma and catalyst produce beneficial results for plasma catalysis, but they also make it difficult to understand the reaction energy mechanism, which must consequently be determined experimentally to obtain sufficient evidence. The energy mechanism depends on various factors, such as reaction species and concentrations, dielectric barrier, and electric fields. Among the factors, the increase in energy utilization in the atmospheric-pressure nonthermal plasma-catalytic reaction must be further elucidated. This paper describes the Energy utilization and kinetic characteristics for several common high-concentration organics, namely $C_5 - C_{10}$ n-alkanes and $(CH_3)_m$-benzenes ($m = 0 - 3$), under the pulsed bipolar plasma-catalytic synergy effect with a focus on the role of reactant structurally steric strain (alkanes) and induction effect (aromatics) in plasma catalysis. Additionally, the kinetics of energy synergy in the pulsed bipolar plasma-catalytic reaction are elaborated, especially for the phenomenon of energy utilization.

Materials and Methodology

Catalyst Preparation

Perovskite-type oxides have excellent properties in plasma discharge and catalysis, such as high temperature resistance, a high dielectric value ($ε = 2000$–10,000), [26] ferroelectricity, [27] and high oxidation and reduction catalytic ability. [28] Among the perovskite-type
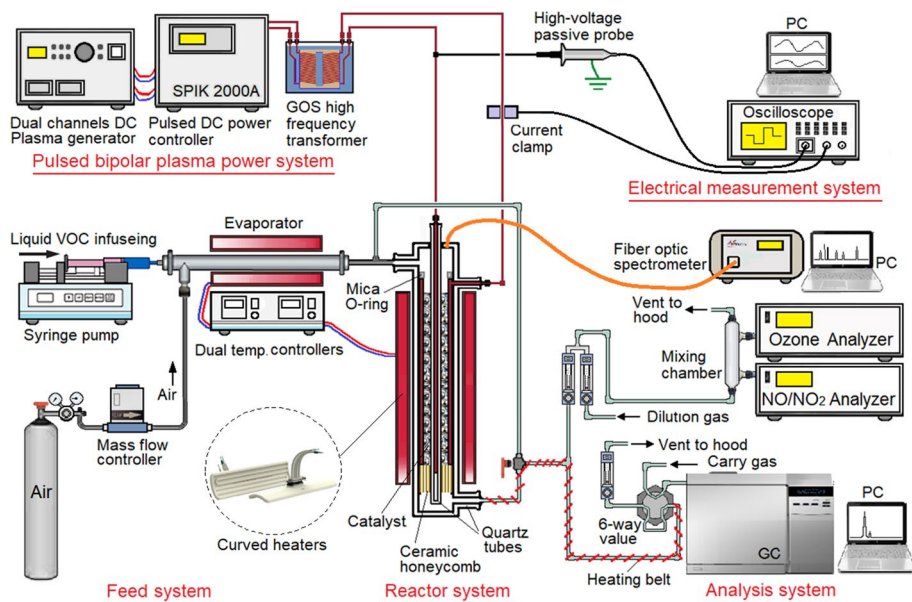
Fig. 1 Schematic of the experimental apparatus

oxides, $La - Sr - Mn - O$ perovskite is the most widely used [29]. Therefore, we employed $La_{0.7}Sr_{0.3}MnO_3$ as the catalyst in this study. A two-stage preparation method was used to prepare $La_{0.7}Sr_{0.3}MnO_3$/mullite catalyst. This preparation method was developed in our previous study. [20] The first stage was calcination at 700 °C by using Kaolin K99-C pellets (diameter: approximately 2 mm) as the raw material of the support to obtain semi-finished mullites. In the second stage, the semi-finished mullites were impregnated with the precursor solution and then calcined at 1100 °C. The precursor solutions contained the starting materials of the perovskite, namely $La(NO_3)_3$, $Sr(NO_3)_2$, and $Mn(NO_3)_3$, in stoichiometric proportions. The nitrate was converted into nitrogen dioxide gas and oxygen during the calcination process. [20] Each gram of supported catalyst pellet contained approximately 0.126 g of $La_{0.7}Sr_{0.3}MnO_3$ catalyst. The X-ray diffraction (XRD) pattern (obtained using a Bruker D2 Phaser XRD) showed that the catalyst had a predominantly perovskite structure. [24] The results of surface characterization performed using a porosimetry analyzer (Micromeritics ASAP 2020) showed that the specific surface area, pore volume, and pore diameter of the $La_{0.7}Sr_{0.3}MnO_3$/mullite catalyst were 1.6778 $m^2\,g^{-1}$, 0.01395 $cm^3\,g^{-1}$, and 52.226 Å, respectively. The results demonstrated the catalyst's strong activity in the plasma catalysis of VOCs, especially at low reaction temperatures. [20, 24]

Reaction Apparatus and Procedures

A schematic of the experimental apparatus is presented in Fig. 1. The apparatus consisted of pulsed bipolar plasma power, electrical measurement, feed, reaction, and analysis systems. The plasma power system was composed of a dual-channel DC generator (ENI DCG-100), pulsed DC power controller (SPIK 2000A), and high-frequency transformer (ShenChang HV-3 K-40–1), which provided the high-frequency pulse bipolar discharge

for plasma catalysis. The electrical measurement system consisted of a four-channel digital storage oscilloscope (Tektronix TBS 1064) with a high-voltage passive probe (Tektronix P6015A) and an AC/DC current probe (Tektronix Tcp-A300) for measuring the applied voltage and plasma current, respectively. The feed system consisted of high-purity (> 99.995%) air cylinders, a mass flow controller, a syringe pump (Stoelting, Model-100), and an evaporator equipped with a proportional–integral–derivative (PID) temperature controller (Shinko, MCD-100). Liquid organic reactants from the syringe pump were mixed with the air stream from the mass flow controller and introduced into the evaporator to prepare the feed gas with a VOC concentration of 4000 ± 100 ppmv. The feed gas was introduced into the plasma-catalytic reactor.

The reaction system comprised a pulsed bipolar atmospheric pressure (PBPAP) plasma-catalytic apparatus, which consisted of a coaxial dielectric barrier discharge plasma-catalytic reactor, furnace (two curved heaters, HCYTECH models FTE and T-FTE), and PID temperature controller. A quartz tube with an inner diameter of 21.4 mm was used as the reactor. A stainless-steel tube (outer diameter: 21 mm, thickness: 1.3 mm, and length: 140 mm) was used as an external electrode, and it was placed in the quartz tube. A mica O-ring and a ceramic honeycomb structure were installed at the upper and lower ends, respectively, of this external electrode as a sealing washer and gas distributor. The internal electrode was a stainless-steel rod with an outer diameter of 4 mm, and it was placed in a bottom-sealed quartz tube of outer diameter 6 mm and thickness 1 mm. This quartz tube also acted as a dielectric barrier layer. An amount of 34.5 g of $La_{0.7}Sr_{0.3}MnO_3/$ mullite catalyst pellet was placed in the gap between the external electrode and dielectric
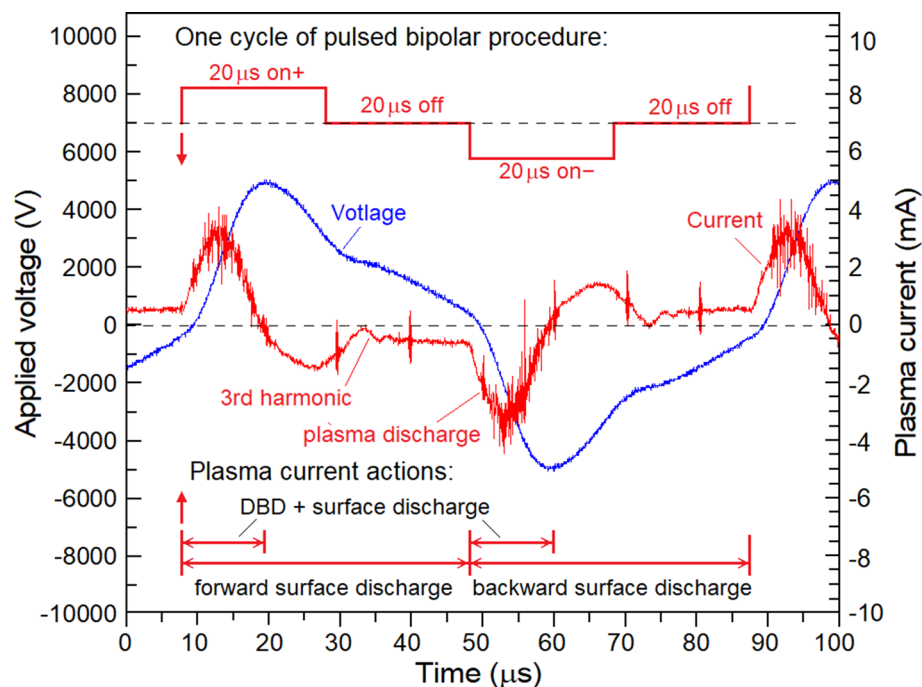
Fig. 2 Schematic of one cycle of pulsed bipolar procedure and the curves of applied voltage and plasma current of air under frequency of 12.5 kHz and atmospheric pressure

layer, and the gas flow rate through this gap was 1 L min^{-1}. The resulting weight hourly space velocity (WHSV) was maintained at 1739 mL h^{-1} g^{-1} of the supported catalyst (or 13,378 mL h^{-1} g^{-1} of the catalyst).

The analysis system comprised an optical emission spectrometer (Avantes, AvaSpec-USB2 Fiber Optical Spectrometer) for obtaining the emission spectra of the element and specie products of plasma catalysis, an ozone analyzer (ShengYi, Ozone Monitor Model-205) for analyzing residual O_3, an NO_x analyzer (API, NO_x Monitor Model-8200A), and a dynamic double-flow dilution set for diluting the gases for analysis. The gases at the inlet and outlet of the plasma-catalytic reactor were analyzed using a gas chromatograph equipped with a flame ionization detector (Shimadzu, GC14B-FID) and a 0.25-mm Chrompack DB-1 60-m-long capillary column. In addition, a gas chromatograph–mass spectrometer (Shimadzu QP-2010 SE GCMS) equipped with another Chrompack DB-1 capillary column was used as an auxiliary unit for the qualitative and quantitative analyses of the products.

Applied Electric Field

The electric fields of NTP reactors have various types of discharge, such as DC/pulsed corona, dielectric barrier, microwave plasma, plasma jet, and gliding arc. [14, 30 − 32] Because pulsed bipolar power (PBP) has higher energy efficiency in terms of generating plasma discharge for plasma catalysis than AC power, [33] atmospheric-pressure PBP was used to treat high-concentration organic waste in this study. In our previous study, the frequency of 12.5 kHz was found to be favorable for supplying energy to the plasma discharge reaction. Figure 2 shows a schematic of one cycle of the pulsed bipolar procedure at 12.5 kHz, with a bipolar cycle of 80 µs. The curves of applied voltage and plasma current are the typical pulsed waveforms of voltage and discharge current, [34] which are not square waves. The plasma current exhibited typical filamentary PBP comprising dielectric barrier discharge and surface discharge.

The specific energy density (SED) of plasma can be defined as the average power (p_{avg}, in W or J s^{-1}) deposited per unit volume of gas flow (Q):
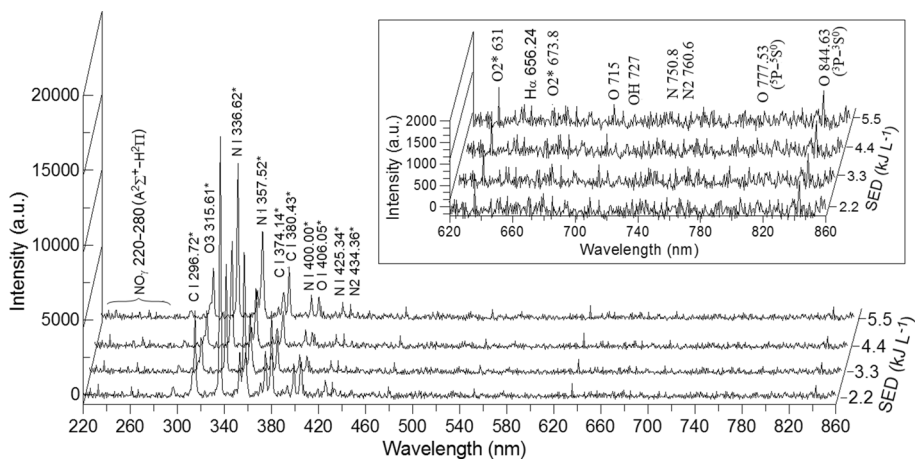

Fig. 3 Optical emission spectra of air over La$_{0.7}$Sr$_{0.3}$MnO$_3$/mullite catalyst in the plasma-catalytic reactor at different applied SEDs

$$SED\left(J\ L^{-1}\right) = \frac{p_{avg}(W)}{Q\left(L\ min^{-1}\right)} \times \frac{60\ s}{min} \tag{1}$$

Nine organic reactants, namely $C_5 - C_{10}$ n-alkanes and $(CH_3)_m$-benzenes ($m = 0 - 3$), were considered the target VOCs in this study. Although the feed concentration of organic compound reached 4000 ppmv, the reaction gas stream mainly consisted of air. Although different organic reactants have differing effects on the intensity of optical emission spectra (OES), they do not alter the spectral pattern. Therefore, the OES of air was selected as the representative for illustrating the products generated (either elements or species) over the $La_{0.7}Sr_{0.3}MnO_3$/mullite catalyst in the pulsed bipolar plasma-catalytic reactor under atmospheric air pressure. Figure 3 shows the OES of air over the $La_{0.7}Sr_{0.3}MnO_3$/mullite catalyst in the plasma-catalytic reactor under different applied SED. The dominant emission peaks were in the wavelength region 310–440 nm, corresponding to emissions from excited O, N, and O_3 atoms, ions, or molecules. The seven minor emission peaks at 406.05, 631.0, 673.8, 715, 727, 777.53, and 844.63 nm represented the excited O atoms, OH radicals, and O_2 molecules. The peak with the maximum intensity was observed at 336.62 nm, and it corresponded to an emission from N I 336.62[*]. In the subsequent work, the intensity of this peak was used as the representative emission for the characterization of optical emission. This was because its intensity was related to the plasma discharge at different reaction temperatures.

Fig. 4 Conversion curves of $C_5 - C_{10}$ alkanes oxidation over $La_{0.7}Sr_{0.3}MnO_3$/mullite catalyst at **a** $SED = 1.02 \pm 0.02$ kJ L^{-1} and **b** $SED = 0$ kJ L^{-1} via the pulsed bipolar plasma-catalytic reactor. The feed concentration of reactants and the weight-hour space velocity (WHSV) were kept at 4000 ± 100 ppmv and 1,739 mL h^{-1} g-supported catalyst $^{-1}$, respectively
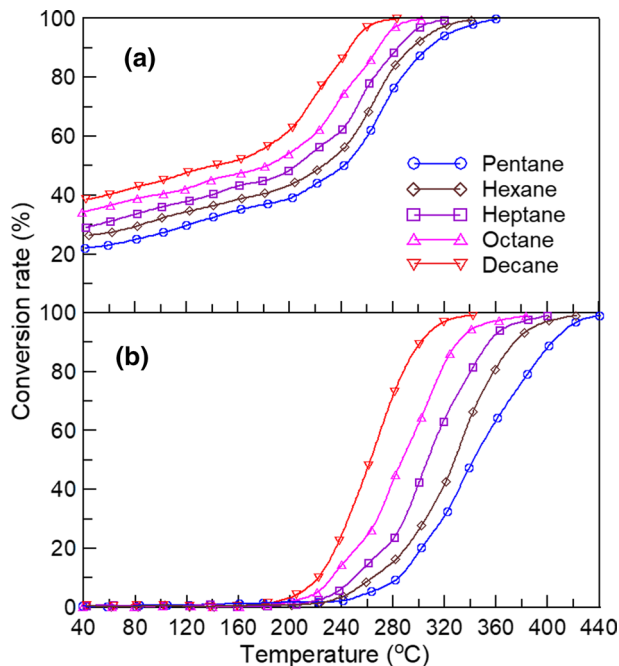
Fig. 5 Residual O_3, NO, and NO_2 concentrations produced by the $C_5 - C_{10}$ n-alkanes after pulsed bipolar plasma-catalytic reactions over the $La_{0.7}Sr_{0.3}MnO_3$/mullite catalyst
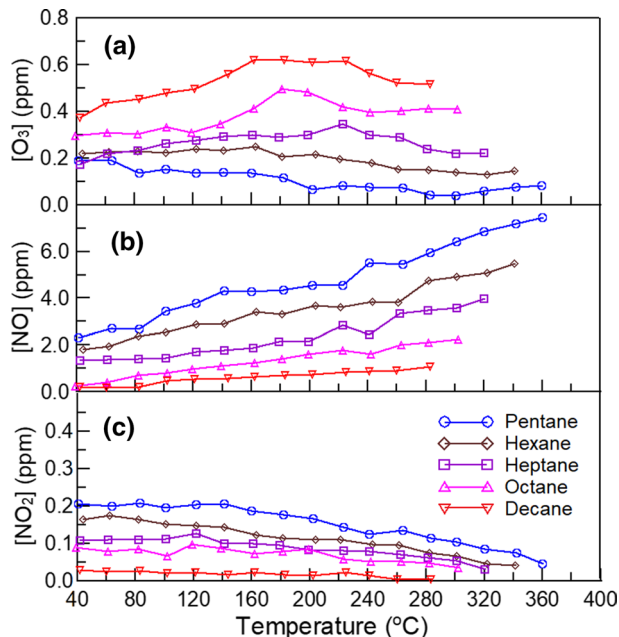
Results and Discussion

Catalysis and Plasma Catalysis of $C_5 - C_{10}$ n-alkanes

For alkanes, differences in reactivity can only be attributed to differences in C–H bond dissociation energy. The bond dissociation energy of alkane depends on its structurally steric strain [35]. The reactivity of hydrogen atoms in organics has the following order: tertiary > secondary > primary. [36] The high numbers of secondary hydrogens in n-alkanes means that they are more easily oxidized. The number of secondary hydrogens (N) in alkanes is $2n - 4$, where n is the carbon number and $n \geq 3$. Figure 4 presents the conversion curves of $C_5 - C_{10}$ n-alkanes in the PBPC reaction over the $La_{0.7}Sr_{0.3}MnO_3$/mullite catalyst at SED $= 1.02 \pm 0.02$ and 0 kJ L^{-1}. According to these curves, the temperatures required for complete catalytic oxidation and plasma-catalytic oxidation decrease as the number of secondary hydrogens in n-alkanes increases. Under the plasma discharge, the conversion rate at 40ºC changed from 22.1% of pentane ($N=6$) to 38.5% of decane ($N=16$). The effects of the number of secondary hydrogens on the catalytic oxidation and plasma-catalytic oxidation will be discussed in subsequent sections.

No organic end- or by-products or CO were detected in this study implying that their concentration is below 0.4 ppmv, the quantification is using the method of semiquantitative analysis by GCMS with a unit in as toluene-ppmv. The concentrations of residual O_3, NO, and NO_2 produced by the $C_5 - C_{10}$ n-alkanes after the pulsed bipolar plasma-catalytic reactions over the $La_{0.7}Sr_{0.3}MnO_3$/mullite catalyst are shown in Fig. 5. Compared with the high concentration of reactants (4000 ± 100 ppmv), the residual amounts of O_3, NO, and NO_2 were low, especially O_3 (<0.62 ppmv) and NO_2 (<0.21 ppm). The residual O_3 concentration increased proportionally as the number of secondary hydrogens in n-alkanes

Fig. 6 Conversion curves of C_m-benzenes ($m = 0 - 3$) oxidation over $La_{0.7}Sr_{0.3}MnO_3$/mullite catalyst at **a** SED $= 1.16 \pm 0.05$ kJ L^{-1} and **b** SED $= 0$ kJ L^{-1} (namely thermal catalysis) via the pulsed bipolar plasma-catalytic reactor. The feed concentration of reactants and the weight-hour space velocity (WHSV) were kept at 4000 ± 100 ppmv and 1,739 mL h^{-1} g-supported catalyst $^{-1}$, respectively
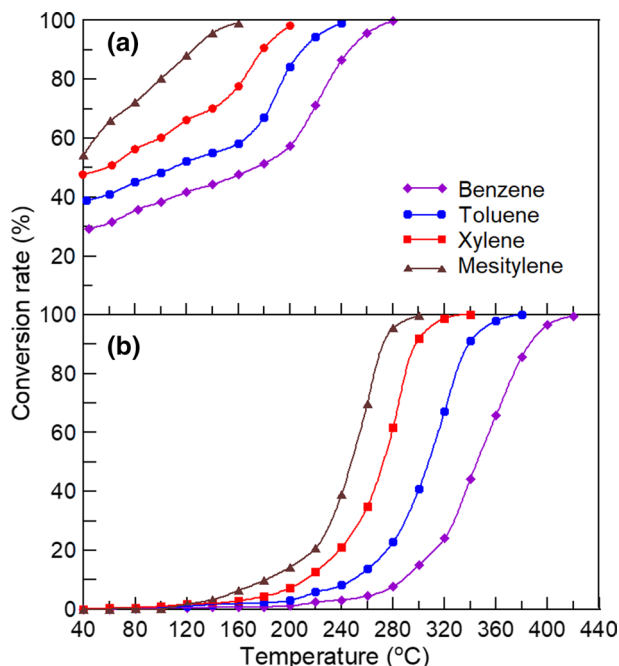
increased. By contrast, the residual concentrations of NO and NO_2 decreased as the number of secondary hydrogens in the n-alkanes increased. The presence of a greater amount

Fig. 7 Residual O_3, NO, and NO_2 concentrations produced by the $(CH_3)_m$-benzenes ($m = 0 - 3$) after pulsed bipolar plasma-catalytic reactions over the $La_{0.7}Sr_{0.3}MnO_3$/mullite catalyst
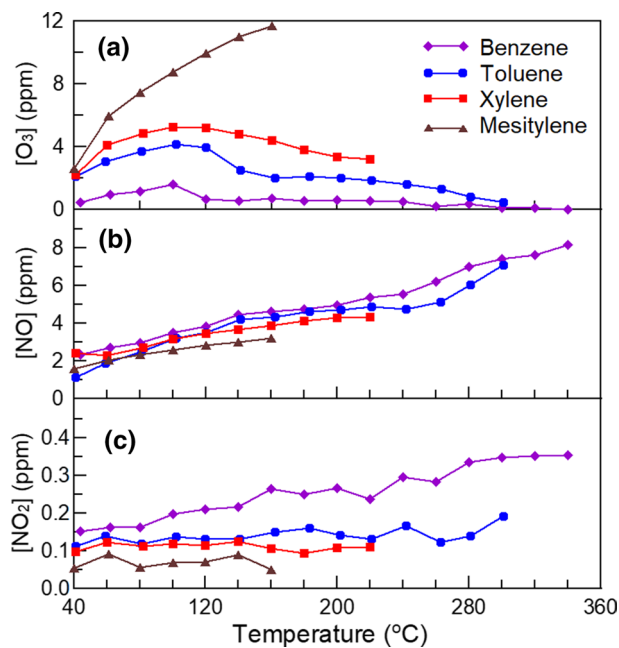
of residual ozone indicated that an organic reactant generated more ozone under plasma discharge, which accelerated its decomposition on the catalyst.

Catalysis and Plasma Catalysis of $(CH_3)_m$-Benzenes

The inductive effect of a molecule is its atom or group transfer electron density through the σ bonds to sp^2-hybridized carbon atoms of benzene ring. Methyl groups donate electron density to the benzene ring through an inductive effect that activates the aromatic ring. Thus, the high proportion of methyl groups in the aromatics indicated that these groups were more easily oxidized. Figure 6 displays the conversion curves of C_m-benzenes in the PBPC reaction over the $La_{0.7}Sr_{0.3}MnO_3$/mullite catalyst at SED $= 1.16 \pm 0.05$ and 0 kJ L^{-1}. The reaction is thermal catalysis when SED $= 0$ kJ L^{-1}. According to the curves, the catalytic reactivity and plasma-catalytic reactivity of the four aromatics were in the following order: mesitylene > xylene > toluene > benzene. And no organic by-products were detected by GCFID or GCMS. When more electrons from more methyl groups are pushed toward the benzene ring, oxidation of the benzene ring is accelerated, especially in plasma catalysis. Aromatics are more easily decomposed than alkanes by plasma discharge at lower temperatures. Owing to the plasma discharge, the conversion rate at 40 °C changed from 37.5% of benzene to 57.2% of mesitylene. The effects of the number of methyl groups on the catalytic oxidation and plasma-catalytic oxidation were extremely strong, which may be attributed to the higher electron density in the benzene ring and is favorable for both the oxidation reactions. This effect will be quantified in subsequent sections.

The concentrations of residual O_3, NO, and NO_2 produced by the C_m-benzenes after the pulsed bipolar plasma-catalytic reactions over the $La_{0.7}Sr_{0.3}MnO_3$/mullite catalyst
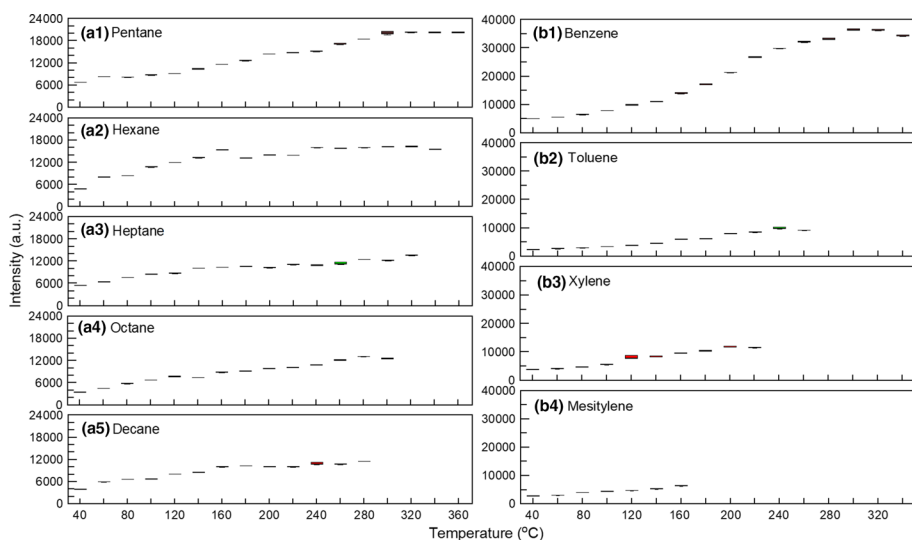
Fig. 8 The relationship between the intensities of N I 336.617* peak and temperatures of (a1−a5) C_5-C_{10} alkanes and (b1−b4) $(CH_3)_m$-benzenes ($m=0-3$) over the $La_{0.7}Sr_{0.3}MnO_3$/mullite, which is using box plot to graphically depict groups of 5 measurements at each reaction temperature

are shown in Fig. 7. Compared to high reactant concentrations (4000 ± 100 ppmv), the amounts of residual O_3, NO, and NO_2 were low. The residual O_3 concentration increased as the number of methyl groups in the aromatic reactants increased, whereas the residual NO and NO_2 concentrations exhibited the reverse trend. These results are similar to those presented in Fig. 5, but the amount of residual ozone after the plasma catalysis of each aromatic reactant was considerably higher than that of each n-alkane. This may be attributed to the higher electron density of the benzene ring that favors shorter on-time pulses, which is more conducive to the formation of ozone in plasma discharge [37]. Thus, the reactivity of the aromatic reactants in plasma catalysis was higher than that of the n-alkanes.

The results in Figs. 5a and 7a show that the residual ozone increased with the increasing secondary hydrogens or methyl groups. The formation of ozone depends on the intensity of plasma discharge, so the residual ozone increased with the increasing secondary hydrogens or methyl groups due to the relative dielectric constants of organic reactants, high dielectric constant is beneficial to plasma discharge intensity. For example, the relative dielectric constants of benzene, toluene, xylene, and mesitylene are about 2.27, 2.38, 2.57, and 3.4, respectively.

Effect of Temperature on the Intensity of Plasma Discharge

As mentioned, the maximum intensity peak of N I 336.62[*] was used as the representative emission for elucidating the optical emission characteristics of VOC plasma catalysis at different reaction temperatures, which was based on using constant applied SED to plasma catalysis of organic reactants. The SED applied to the five alkanes and four aromatics was 1.02 ± 0.02 and 1.16 ± 0.05 kJ L^{-1}, respectively. The relationship between the intensity of the N I 336.62[*] peak and temperature is illustrated in Fig. 8. The results indicated that the plasma discharge intensity was influenced by the reactant and temperature. Low-reactivity organic reactants required higher reaction temperature. Therefore, the plasma discharge versus temperature curve exhibited higher intensity at 40ºC and a higher rate of increase, especially for benzene (Fig. 8b1). When the reactant conversion rate was close to 100%, the plasma discharge intensity gradually flattened out or slightly decreased. Therefore, the presence of organic reactants enhanced the plasma discharge. At high reaction temperatures, large quantities of low-reactivity reactants were present, and therefore, the plasma discharge intensity was high. A comparison of the amount of residual ozone (Figs. 5a and 7a) with the plasma discharge intensity (Fig. 8) revealed an inverse relationship, possibly because when the applied energy was used to generate more ozone, the intensity of the plasma discharge decreased. Therefore, the plasma catalysis of organic reactants was dominated by large quantities of ozone rather than high plasma discharge intensity. In addition, the intensity of plasma discharge is function of the equivalent capacitance of reactant and product gases strongly, which will depict in our follow-up study.

Kinetics of Catalysis Alone

For catalysis alone, the reaction rate of catalytic oxidation can be expressed as follows: [24, 38]

$$\frac{dC}{dt} = -kSC = -k_c C \tag{2}$$
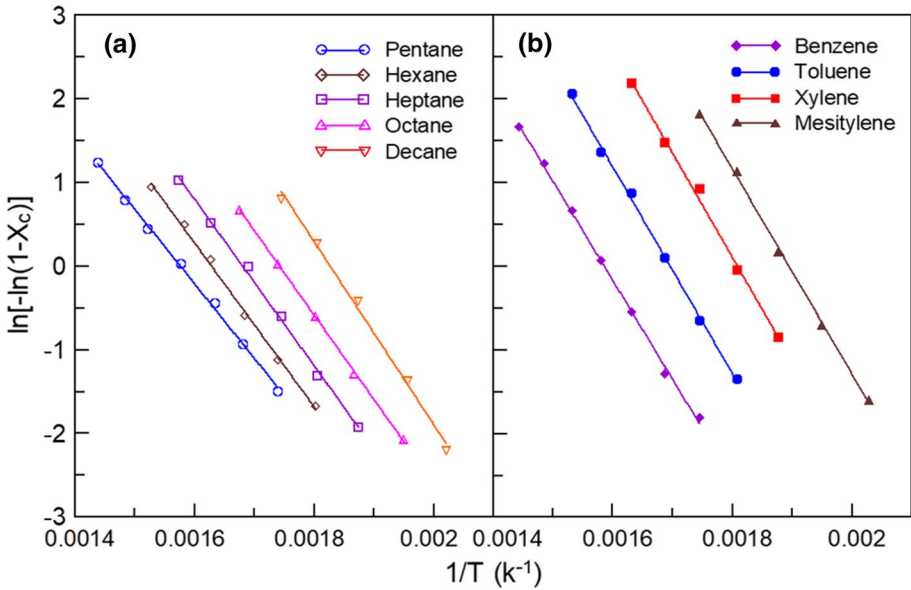
Fig. 9 Plot of $\ln[-\ln(1-X_c)]$ versus $1/T$ for the oxidation of **a** C_5-C_{10} alkanes and **b** $(CH_3)_m$-benzenes ($m=0-3$) over the $La_{0.7}Sr_{0.3}MnO_3$ catalyst/mullite, from which their $-b$ and $\ln a$ values are obtained

Table 1 Summary the kinetic parameters of the nine organic reactions in the catalysis over the $La_{0.7}Sr_{0.3}MnO_3$/mullite catalyst

Reactants	$\ln a$	b	k_o (s^{-1})	E_a (kcal mole^{-1})	R^2
Alkanes					
Pentane	14.046	8910	1.66×10^5	17.70	0.995
Hexane	15.945	9792	1.11×10^6	19.46	0.998
Heptane	16.724	99,521	2.41×10^6	19.77	0.998
Octane	17.575	10,063	5.65×10^6	20.00	0.997
Decane	20.144	11,028	7.37×10^7	21.91	0.995
Aromatics					
Benzene	18.782	11,841	1.89×10^7	23.53	0.998
Toluene	20.956	12,353	1.66×10^8	24.55	0.998
Xylene	22.530	12,455	8.01×10^8	24.75	0.996
Mesi-tylene	23.248	12,267	1.64×10^9	24.37	0.999

where C is the reactant concentration, S is an adsorption site on the catalyst surface, and the apparent rate constant $k_c = kS$. Equation (2) can be integrated as

$$\frac{C}{C_0} = e^{-k_c t} \tag{3}$$

where C and C_o respectively denote the reactant concentrations at the reaction times $t=t$ and $t=0$, The expression of the conversion rate X_c is as follows:

$$X_c = 1 - \frac{C}{C_0} = 1 - e^{-k_c t} \tag{4}$$

The apparent rate constant can be calculated using the Arrhenius law as follows:

$$k_c = k_0 e^{-\frac{Ea}{RT}} \tag{5}$$

where E_a, R, T, and k_o denote the activation energy, gas constant, temperature, and pre-exponential factor of the reaction, respectively. Rearranging and applying the natural logarithm to this expression yields the following:

$$\ln\left[-\ln\left(1 - X_c\right)\right] = \ln a - \frac{b}{T} \tag{6}$$

where $a = k_o t$ and $b = E_a/R$. Equation (6) yields a straight line, as in the graph of $1/T$ versus $\ln[-\ln(1-X)]$ with the intercept being $\ln a$ and the slope being b, from which k_o and E_a can be calculated. In this study, the reaction time $t = V/Q = 0.1267$ L / 1 L $\min^{-1} = 0.1267$ min $= 7.6$ s, where V denotes the volume of the catalyst bed. Figure 9 shows plots of $\ln[-\ln(1-X_c)]$ versus $1/T$ for the oxidation of C_5-C_{10} alkanes and C_x-benzenes over the $La_{0.7}Sr_{0.3}MnO_3$/mullite catalyst. Table 1 presents a summary of the kinetic parameters of the nine organic reactions in the catalysis. The results show that $\ln a$ and b increase as the numbers of secondary hydrogens and methyl groups increase. The ranges for C_5-C_{10} n-alkanes and $(CH_3)_m$-benzenes ($m = 0-3$) are $17.70-21.91$ and $23.53-24.75$ kcal mol^{-1}, respectively. As the number of secondary hydrogens in alkanes or number of methyl groups in monocyclic aromatics increased, k_o increased exponentially, which is consistent with the results presented in Figs. 4b and 6b.

Kinetics of Plasma Catalysis with Energy Synergy

Plasma-catalytic reactions involve plasma dissociation of the reaction gas flowing between the electrodes and catalysis of the dissociated products (active species such as excited atoms, ions, and molecules) combined with undissociated reactants. The active species can enhance the catalysis process by participating in the reaction, which is favorable for oxidation of the reactants. Thus, the catalysis in a PDC system is a synergistic process, and its strength depends on the applied SED and temperature. The overall plasma-catalytic reaction can be construed as plasma dissociation and synergistic catalysis:

$$r_{\text{overall}} = r_{\text{plasma dissociation}} + r_{\text{synergistic catalysis}} \tag{7}$$

The differential rate formula of Eq. (7) is as follows:

$$\frac{dC}{C} = -k_E dSED - k_{SC} dt \tag{8}$$

where k_E and k_{SC} are the rate constant of plasma dissociation (L kJ^{-1}) and the apparent rate constant of synergistic catalysis (s^{-1}), respectively. Integration of Eq. (8) yields the following:

$$\ln\frac{C}{C_o} = -k_E SED - k_{SC} t \tag{9}$$

The overall conversion rate X_{PC} of plasma catalysis can be described as follows:

$$X_{PC} = 1 - \frac{C}{C_0} = 1 - \exp\left(-k_E SED - k_{SC} t\right) \tag{10}$$

The rate equation of plasma dissociation alone is as follows [39, 40]:

$$\frac{dC}{C} = -k_E dSED \tag{11}$$

Equation (11) can be integrated to obtain the conversion rate formula of plasma dissociation alone:

$$\frac{C}{C_0}\bigg|_p = e^{-k_E \cdot SED} \text{ or } X_p = 1 - \frac{C}{C_0}\bigg|_p = 1 - e^{-k_E \cdot SED} \tag{12}$$

where the subscript p indicates that the reaction involves only plasma dissociation. Rearranging and applying the natural logarithm to Eq. (12) yields the following:

$$k_E = -\frac{\ln\left(1 - X_p\right)}{SED} \tag{13}$$

As mentioned, the strength of plasma dissociation depends on the applied SED and temperature. Thus, Eq. (13) can be described as a function of SED and T:

$$k_E = -\frac{\ln\left(1 - X_p\right)}{SED} = k_{E0} + k_{E1} \cdot T + k_{E2} \cdot SED \tag{14}$$
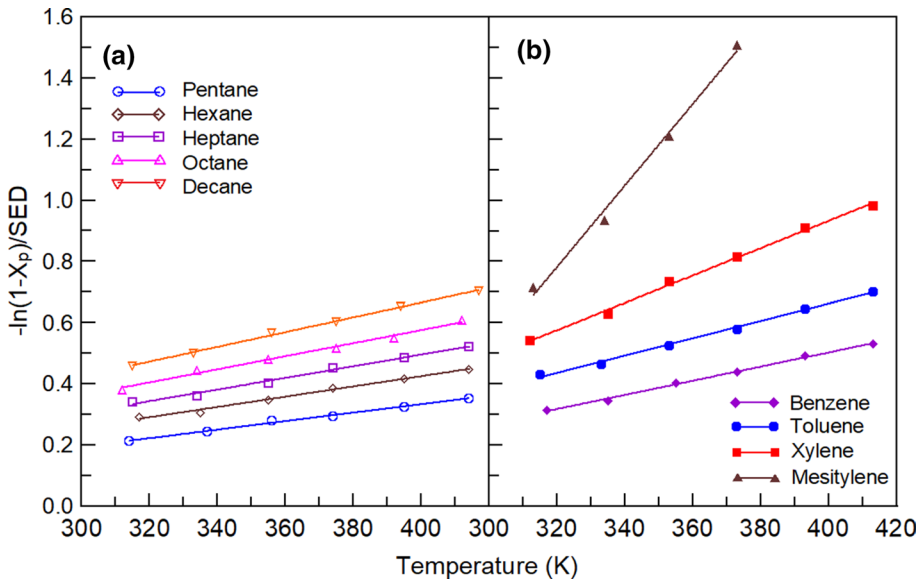
Fig. 10 Plot of apparent energy constants ($k_E = -\ln(1 - X_p)/SED$, L kJ^{-1}) versus at T (K) for the plasma-catalytic reactions of **a** C$_5$–C$_{10}$ alkanes at SED$=1.02\pm0.02$ kJ L^{-1} and **b** (CH$_3$)$_m$-benzenes ($m=0-3$) at SED$=1.16\pm0.05$ kJ L^{-1} over La$_{0.7}$Sr$_{0.3}$MnO$_3$/mullite catalyst

where k_{E0}, k_{E1}, and k_{E2} are the coefficients of the multivariate equation. When SED is constant, Eq. (14) can be simplified to the following form:

$$k_E = -\frac{\ln(1-X_p)}{SED} = k_{E0} + k_{E1} \cdot T \tag{15}$$

Equation (15) represents a straight line in the graph of $-\ln(1-X_p)/SED$ versus T with the intercept being k_{E0} and slope being k_{E1}, from which k_{E0} and g k_{E1} can be obtained. Figure 10 presents the plots of $-\ln(1-X_p)/SED$ versus T for the plasma dissociation of the organic reactants over the $La_{0.7}Sr_{0.3}MnO_3$/mullite catalyst. The results shown in Figs. 4 and 6 indicate that catalysis was not evident at temperatures lower than 120 °C, and only plasma dissociation may have occurred. Therefore, the data obtained at temperature ≤ 120 °C were fitted using Eq. (14) to determine the coefficients k_{E0} and k_{E1} for the given SED and T values. Figure 10 shows plots of the apparent energy constants ($k_E = -\ln(1-X_p)/SED$, L kJ^{-1}) versus at T (K) for the plasma-catalytic reactions of the nine organic reactants over the $La_{0.7}Sr_{0.3}MnO_3$/mullite catalyst.

Synergistic catalysis comprises catalysis and energy synergy. The ratio of energy ($R \times T$) terms is a quantitative index that can be used to evaluate the synergy effect. In our previous research, [24] the synergy factor Ψ_X was defined to evaluate the energy synergy effect as follows:

$$\text{Synergy factor} \psi_X = \frac{T_{X,\text{cal}}}{T_{X,\text{exp}}} \tag{16}$$

where $T_{X,\text{exp}}$ and $T_{X,\text{cal}}$ denote the experimental temperature in the plasma catalysis and calculated temperature in the PEC for the conversion X of the reactant, respectively. The formula for computing $T_{X,\text{cal}}$ is as follows: [20]

$$T_{X,cal} = \frac{b}{\ln a - \ln\{-[\ln(1-X) + k_E \cdot SED]\}} \tag{17}$$

where Ψ_X is constant throughout the plasma-catalytic reaction, so it expressed as Ψ in the subsequent equations. In this study, the synergy factor was obtained using the ratio of both temperatures at the conversion rate of 80% ($T_{80,\text{exp}}$ and $T_{80,\text{cal}}$), because synergistic catalysis

Table 2 Summary the kinetic parameters of the nine organic reactions in the PBPAP plasma catalysis over the $La_{0.7}Sr_{0.3}MnO_3$/mullite catalyst

Reactants	k_{E0} (L kJ^{-1})	k_{E1} (L kJ^{-1} K^{-1})	R^2	Ψ
Alkanes at $SED = 1.02 \pm 0.02$ kJ L^{-1}				
Pentane	− 0.234	1.458×10^{-3}	0.994	1.04
Hexane	− 0.258	1.760×10^{-3}	0.991	1.04
Heptane	− 0.278	1.994×10^{-3}	0.992	1.04
Octane	− 0.292	2.240×10^{-3}	0.990	1.03
Decane	− 0.312	2.524×10^{-3}	0.998	1.04
Aromatics at $SED = 1.16 \pm 0.05$ kJ L^{-1}				
Benzene	− 0.389	2.131×10^{-3}	0.996	1.17
Toluene	− 0.431	2.603×10^{-3}	0.996	1.17
Xylene	− 0.786	4.116×10^{-3}	0.997	1.18
Mesitylene	− 3.212	1.230×10^{-2}	0.993	1.19
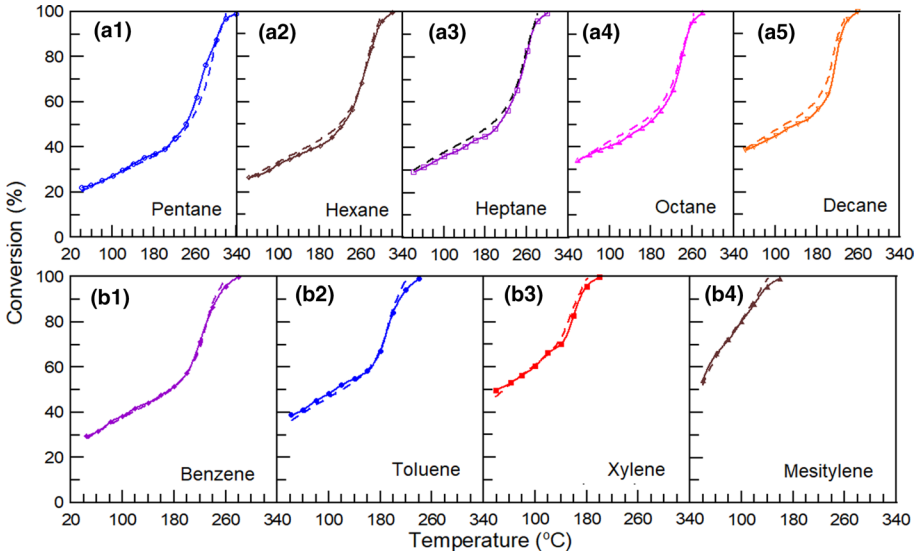
Fig. 11 Comparison of the conversion–temperature curves between theoretical and experimental results of a1 − a5 alkanes and b1 − b4 msonocyclic aromatics over $La_{0.7}Sr_{0.3}MnO_3$/mullite catalyst. Solid and dashed lines are the theoretical and experimental results, respectively

was dominant over catalysis. Thus, Eq. (5) can be rewritten as the following expression for determining k_{SC} in synergistic catalysis:

$$k_{SC} = k_0 e^{-\frac{E_a}{RT_{90,T}}} \text{ or} k_{SC} = a\exp\left(-\frac{b}{T}\right) \qquad (18)$$

By substituting Eq. (18) into Eq. (10), the theoretical equation of plasma catalysis can be obtained as follows:

$$X_T = 1 - \exp\left[-\left(k_{E0} + k_{E1} \cdot T\right)SED - a\exp\left(\frac{-b}{T \cdot \psi}\right)\right] \qquad (19)$$

Equation (19) can be used to predict the conversion rate X_T for the plasma catalysis of organic reactants at various SED and T. Table 2 shows the kinetic parameters of the nine organic reactions in the PBPAP plasma catalysis over the $La_{0.7}Sr_{0.3}MnO_3$/mullite catalyst. The applied SED for the five alkanes and four aromatics was 1.02 ± 0.02 and 1.16 ± 0.05 kJ L^1, respectively. The results indicate that k_{E0} and k_{Ea} increased as the number of secondary hydrogens or methyl groups increased, especially for mesitylene. The synergy factor of the five alkanes was approximately 1.04, which indicates that the reaction was independent of the number of secondary hydrogens. As the number of methyl groups increased, k_{E0} and k_{Ea} increased, leading to corresponding increases in the synergy factors of the four aromatics.

Comparison of Theoretical and Experimental Results

The kinetic parameters of the plasma catalysis of the nine organic reactants with the $La_{0.7}Sr_{0.3}MnO_3$/mullite catalyst are listed in Tables 1 and 2. These parameters were used
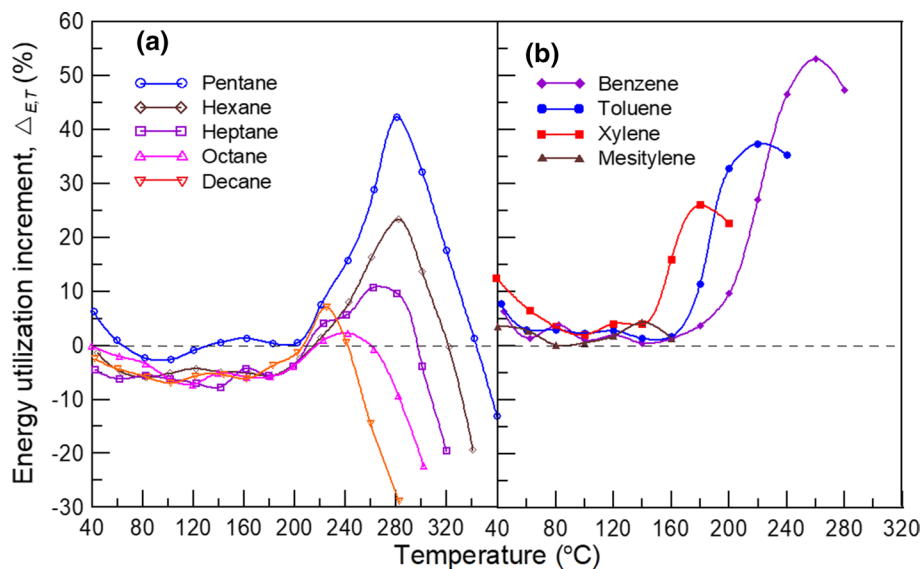
Fig. 12 The relationship between the energy utilization increment of synergy effect and reaction temperature of **a** the five alkanes (at $SED = 1.02 \pm 0.02$ kJ L^{-1}) and **b** the four aromatics (at $SED = 1.16 \pm 0.05$ kJ L^{-1}) in the PBPAP plasma catalysis over La$_{0.7}$Sr$_{0.3}$MnO$_3$/mullite catalyst

to obtain theoretical conversion–temperature curves by using Eq. (19). Figure 11 displays the theoretical and experimental results of the nine organic reactants obtained using the La$_{0.7}$Sr$_{0.3}$MnO$_3$/mullite catalyst in the PBPAP plasma catalysis reaction. According to these results, the relative error was extremely small for the oxidation of each organic reactant, especially for the plasma catalysis of the four aromatics. The theoretical equation could be used to explain the behavior of plasma dissociation and synergistic catalysis in the plasma catalysis of organic waste gas and accurately predict conversion–temperature curves. Thus, the equation is useful for designing practical measures for controlling air pollution.

Energy Utilization Characteristics

For plasma catalysis of organic reactants, the conversion energy in the reactor is supplied by the applied SED and heat. The applied SED and heat initiate the plasmolysis and catalysis of the reaction gas, respectively. A higher rate of utilization of the conversion energy amounts to higher conversion efficiency. Therefore, the conversion energy required for the reaction is proportional to the rate of energy utilization. On the basis of this concept, an increase in energy utilization due to the energy synergy effect at the same temperature can be defined as $\Delta_{E,T}$:

$$\Delta_{E,T}(\%) = \frac{X_{s,T} - \left(X_{p,T} + X_{c,T} \right)}{X_{p,T} + X_{c,T}} \times 100 \tag{20}$$

where $X_{s,T}$, $X_{p,T}$, and $X_{c,T}$ denote the conversion rates due to the energy synergy, plasma dissociation alone, and catalysis alone at temperature T, respectively. Because the catalyst also serves as the dielectric barrier material, plasma dissociation alone cannot occur in the absence of the catalyst. Therefore, we estimated $X_{p,T}$ using Eq. (12) to obtain a conversion rate in the absence of catalysis.

Figure 12 illustrates the relationship between the increase in energy utilization due to the synergy effect and reaction temperature for the five alkanes and four aromatics in the plasma catalysis reaction over the $La_{0.7}Sr_{0.3}MnO_3$/mullite catalyst. The SED values applied in the plasma catalysis of the alkanes and aromatics were 1.02 ± 0.02 and 1.16 ± 0.05 kJ L^{-1}, respectively. The results indicated that the increase in the energy utilization rate due to the synergy effect was inversely proportional to the plasma-catalytic reactivity of the organic reactant. Therefore, in terms of the increase in the energy utilization rate, plasma catalysis is favorable for the removal of organic waste gases that are not easily oxidized. The increase in the energy utilization rate of alkanes was low (or even negative) and inconsistent when the reaction temperature was less than 200 °C (overall conversion rate $X_{PC} < 50\%$, except for decane; see Fig. 4a). When the conversion rate was higher than 75%, the increase in the energy utilization rate was significantly smaller. The rate of increase in energy utilization for aromatics was also low and inconsistent when the reaction temperature was less than 140ºC, but it remained positive for all the aromatics. As illustrated in Fig. 12a, the rate of increase in energy utilization significantly decreased, but X_{PC} for the plasma catalysis of the aromatics was higher than 95% (Fig. 6a). Therefore, part of the energy supplied by the plasma discharge or heating was wasted at low and high X_{PC}. When the catalytic activity began to play a role, the active species (excited atoms, ions, or molecules) generated through plasma dissociation greatly accelerated the catalytic reaction. Thus, synergistic catalysis occurred. In addition, when the reaction temperature was close to the complete oxidation temperature, the plasma dissociation and catalysis reactions competed with each other, resulting in wastage of some of the energy. This phenomenon was more pronounced for the n-alkanes than for the monocyclic aromatics.

Conclusions

High proportion of secondary hydrogens in alkanes and high amount of methyl groups in aromatics indicate that are more easily oxidized, which are attributed to their lower bond dissociation energy and higher inductive effect, respectively. In this study, we systematically investigated the plasma dissociation and synergistic catalysis of the alkanes and aromatics based on their kinetic characterizations in the PBPAP plasma catalysis reaction. The induced effect of the methyl group weakened the conjugated benzene ring and made it more susceptible to destruction by plasma discharge. Thus, the synergy factor of the aromatics increased as the number of methyl groups increased. The activities of the five alkanes were dependent of the number of secondary hydrogens, but their synergy factor does not increase accordingly. These results demonstrate that the effect of reactant structurally bond strength and inductive effect on synergy factor of plasma-catalytic reaction are slightly and obviously, respectively. The calculation results obtained using the established theoretical formula revealed that the relative error was small for the oxidation of each organic reactant, especially for the plasma catalysis of the four

aromatics. Moreover, the increase in energy utilization due to the synergy effect was inversely proportional to the reactivity of the organic reactants. Some of the energy supplied by the plasma discharge or heating was wasted at low X_{PC} until the catalytic activity began to play a role. The increase in energy utilization was remarkable when catalytic activity at work. When the reaction temperature was close to the complete oxidation temperature, plasma dissociation and catalysis competed with each other, resulting in the loss of some of the supplied energy. These phenomena were more pronounced for the n-alkanes than for the monocyclic aromatics.

Declarations

Conflict of interest The authors declare that they have no conflict of interest.

References

1. Markiewicz A, Björklund K, Eriksson E, Kalmykova Y, Strömvall AM, Siopi A (2017) Emissions of organic pollutants from traffic and roads: Priority pollutants selection and substance flow analysis. Sci Total Environ 580:1162–1174
2. Adam TW, Astorga C, Clairotte M, Duane M et al (2011) Chemical analysis and ozone formation potential of exhaust from dual-fuel (liquefied petroleum gas/gasoline) light duty vehicles. Atmos. Environ. 45:2842–2848
3. Elliott MA, Nebel GJ, Rounds FG (2012) The composition of exhaust gases from diesel, gasoline and propane powered motor coaches. J Air Pollut Control Assoc 5(2):103–109
4. Xiong Y, Du K (2020) Source-resolved attribution of ground-level ozone formation potential from VOC emissions in Metropolitan Vancouver. BC Sci Total Environ 721:137698
5. Chen CH, Chuang YC, Hsieh CC, Lee CS (2019) VOC characteristics and source apportionment at a PAMS site near an industrial complex in central Taiwan. Atmos Pollut Res 10:1060–1074
6. Liang CW, Ku CK, Liang JJ (2013) The scale-free network behavior of ambient volatile organic compounds. Environ Sci Pollut Res 20:872–883
7. Jobson BT, Berkowitz CM, Kuster WC, Goldan PD, Williams EJ, Fesenfeld FC, Apel EC, Karl T, Lonneman WA, Riemer D (2004) Hydrocarbon source signatures in Houston, Texas: influence of the petrochemical industry. J Geophys Res Atmos 109:24305–24326
8. Zheng H, Kong S, Yan Y, Chen N, Yao L, Liu X, Wu F, Cheng Y, Niu Z, Zheng S, Zeng X, Yan Q, Wu J, Zheng M, Liu D, Zhao D, Qi S (2020) Compositions, sources and health risks of ambient volatile organic compounds (VOCs) at a petrochemical industrial park along the Yangtze River. Sci Total Environ 703:135505
9. Jiang J, Feng X, Yang M, Wang Y (2020) Comparative techno economic analysis and life cycle assessment of aromatics production from methanol and naphtha. J Clean Prod 27:123525
10. Ma L, He M, Fu P, Jiang X, Lv W, Huang Y, Liu Y, Wan H (2020) Adsorption of volatile organic compounds on modified spherical activated carbon in a new cyclonic fluidized bed. Sep Purif Technol 235:116146
11. Lee JE, Ok YS, Tsang DCW, Song JH, Jung SC, Park YK (2020) Recent advances in volatile organic compounds abatement by catalysis and catalytic hybrid processes: a critical review. Sci Total Environ 719:137405
12. Salvador S, Commandré JM, Kara Y (2006) Thermal recuperative incineration of VOCs: CFD modelling and experimental validation. Appl Therm Eng 26:2355–2366
13. Whitehead JC (2019) Plasma-catalysis: Is it just a question of scale? Front Chem Sci Eng 13(2):264–273
14. Kim HH (2004) Nonthermal plasma processing for air-pollution control: a historical review, current issues, and future prospects. Plasma Process Polym 1:91–110
15. Holzer F, Roland U, Kopinke FD (2002) Combination of non-thermal plasma and heterogeneous catalysis for oxidation of volatile organic compounds Part 1. Accessibility of the intra-particle volume. Appl. Catal. B-Environ. 38:163–181

16. Gervasini A, Vezzoli G, Ragaini V (1996) VOC removal by synergic effect of combustion catalyst and ozone. Catal Today 29:449–455
17. Einaga H, Ibusuki T, Futamura S (2001) Performance evaluation of a hybrid system comprising silent discharge and manganese oxide catalysts for benzene decomposition. IEEE Trans Ind Appl 37:1476–1482
18. Jarrige J, Vervisch P (2009) Plasma-enhanced catalysis of propane and isopropyl alcohol at ambient temperature on a MnO_2-based catalyst. Appl Catal B-Environ 90(1–2):74–82
19. Lin BY, Chang MB, Chen HL, Lee HM, Yu SJ, Li SN (2011) Removal of C_3F_8 via the combination of non-thermal plasma, adsorption and catalysis. Plasma Chem Plasma P 31:585–594
20. Liang CJ, Li KW (2018) Kinetic characterization of plasma-enhanced catalysis of high-concentration volatile organic compounds over mullite supported perovskite catalysts. J Electrostat 96:134–143
21. Xg Dang C, Qin JH, Teng J, Huang X (2016) Adsorbed benzene/toluene oxidation using plasma driven catalysis with gas circulation: Elimination of the byproducts. J Ind Eng Chem. 37:366–371
22. Kim HH, Ogata A, Futamur S (2006) Effect of different catalysts on the decomposition of VOCs using flow-type plasma-driven catalysis. IEEE T Plasma Sci 34(3):984–995
23. Kim HH, Ogata A (2011) Nonthermal plasma activates catalyst: from current understanding and future prospects. Eur Phys J Appl Phys 55:13806
24. C J Liang, Z Y Lee, 2020 Kinetic investigation of energy synergy in the pulsed bipolar plasma-catalytic reaction of organic waste gases over mullite-supported perovskite catalysts. *Plasma Chem Plasma P.* 40: 883–906.
25. Li J, Ma C, Zhu S, Yu F, Dai B, Yang D (2019) A review of recent advances of dielectric barrier discharge plasma in catalysis. Nanomaterials 9:1428
26. Sahu T, Patra AK, Behera B (2017) Effect of gadolinium doping on structural, ferroic and electrical properties of 0.8BiGdxFe1−xO3–0.2PbTiO3 (x = 0.00, 0.05, 0.10, 0.15 and 0.20) composites. J Alloys Compd 695:2273–2284
27. Gao W, Zhu Y, Wang Y, Yuan G, Liu JM (2020) A review of flexible perovskite oxide ferroelectric films and their application. J Materiomics 6:1–16
28. Liang CJ, Fang JW (2016) Predicting the kinetics of catalytic oxidation of multicomponent organic waste gases. Chem Eng Sci 144:101–107
29. Wang W, Yuan F, Niu X, Zhu Y (2016) Preparation of Pd supported on La(Sr)-Mn-O perovskite by microwave irradiation method and its catalytic performances for the methane combustion. Sci Rep 6:19511
30. Chen HL, Lee HM, Cheng LC, Chang MB, Yu SJ, Li SN (2008) Influence of nonthermal plasma reactor type on CF_4 and SF_6 abatements. IEEE Trans Plasma Sci 36:509–515
31. Uhm HS, Hong YC (2011) Various micro plasma jets and their sterilization of microbes. Thin Solid Films 519:6974–6980
32. Lee DH, Kim KT, Cha MS, Song YH (2007) Optimization scheme of a rotating gliding arc reactor for partial oxidation of methane. Proc Combust Inst 31:3343–3351
33. Yuan D, Tang S, Qi J, Li N, Gu J, Huang H (2017) Comparison of hydroxyl radical generation during granular activated carbon regeneration in DBD reactor driven by bipolar pulse power and alternating current power. Vacuum 143:87–94
34. M H Chiang, K C Liao, I M Lin, C C Lu, H Y Huang, C L Kuo, J S Wu, C C Hsu, S H Chen, 2010 Effects of oxygen addition and treating distance on surface cleaning of ITO Glass by a non-equilibrium nitrogen atmospheric-pressure plasma jet. Plasma Chem Plasma P 30: 553–563.
35. Wilson EK (2006) Explaining C-H bond strengths: alternative to hyperconjugation invokes steric strain, but not everyone is buying the idea. Chem Eng News 84(10):65
36. Long AK, Fawcett JA, Clyburne JAC, Pye CC (2016) RADMAP: Simple probes for rapid assessment of complex reactivity: a method and case studies on the reaction of hydrogen atoms with unsaturated organic molecules. J Mol Graph Model 64:147–152
37. Liang CJ, Lee ZY (2020) Effects of oxygen-containing functional groups on the synergy effect in pulsed bipolar plasma-catalytic reactions of volatile organic compounds. RSC Adv 10:11400
38. Montazersadgh F, Wright A, Ren J, Shaw A, Neretti G, Bandulasena H, Iza F (2019) Influence of the on-time on the ozone production in pulsed dielectric barrier discharges. Plasma 2:39–50
39. Li J, Sun W, Pashaie B, Dhali SK (1995) Streamer discharge simulation in flue gas. IEEE Trans Plasma Sci 23:672–678
40. Kim HH, Prieto G, Takashima K, Katsura S, Mizuno A (2002) Performance evaluation of discharge plasma process for gaseous pollutant removal. J Electrost 55:25–41

Authors and Affiliations

Chen-Jui Liang[1] · Kuan-Yu Huang[2]

✉ Chen-Jui Liang
    cjliang@fcu.edu.tw

[1] International School of Technology and Management, Feng Chia University, Taichung, Taiwan

[2] Department of Materials Science and Engineering, Feng Chia University, Taichung, Taiwan